Long-term Fluid Injection Can Expedite Fault Reactivation and Development: Riedel Shear Structures Illuminated by Induced Earthquakes in Alberta, Canada

Hongyu Yu[1*], Honn Kao[1, 2], Bei Wang[1, 2], and Ryan Visser[3]

[1] Geological survey of Canada, Sidney, British Colombia, Canada, V8L 5T5

[2] University of Victoria, Victoria, British Colombia, Canada, V8P 5C2

[3] Geoscience BC, Vancouver, BC, Canada, V6B 1R6

Abstract

Riedel shear structures (RSS) are often observed in the embryonic stage of strike-slip fault development, which can be depicted in the field through outcrops and co-seismic surface ruptures. It is a critical concept linking the geomechanical behavior of individual earthquakes to structural geology at both local and regional scales. However, the influence of long-term fluid injections on the developing process of RSS, as manifested by the common occurrences of injection-induced earthquakes, has been rarely addressed. Here we document for the first time subsurface RSS expedited by long-term wastewater disposal injections in western Canada. We study an earthquake sequence consisting of 187 events (M_L ranging 1.3–3.9) between 2018/01/01 and 2021/07/15 in an area without any previous seismic history. According to 31 well-constrained focal mechanism solutions, the injection-related earthquake sequence exhibits various faulting types with the vast majority (87%) being compatible with the background stress regime. The orientation of derived nodal planes collectively indicates a model of RSS that consists of four primary strike-slip structures striking 19º (R'), 79º (R), 94º (PDZ) and 109º (P), respectively. Moreover, six fault segments delineated from the relocated local seismicity are parallel to the sub-structures of RSS. Mohr-Coulomb failure analysis further suggests a cumulative stress perturbation of up to 10.0 MPa. Our observations suggest that long-term fluid injection can expedite the development of local fault systems. Therefore, it is probably important to consider the dimension of local/regional RSS in the assessment of the overall seismic hazard due to fluid injections.

Plain Language Summary

Under a shear stress regime, randomly distributed small fault segments would evolve into a mature strike-slip fault system. During the early stage, a network of shear structures with favored orientations for rupturing are often observed, called Riedel shear structures (RSS). The depiction of RSS can help understand the geomechanical behavior of individual earthquakes. It is well accepted that long-term fluid injections can cause earthquakes, yet their influence on the developing process of RSS is rarely discussed. Here we document a clear case in western Canada where the development of a local RSS system is expedited by 25 years of wastewater injection. The RSS system is manifested by an earthquake sequence consisting of 187 small-to-moderate-sized events. Focal mechanisms of these events exhibit various faulting types with the majority being compatible with the background stress regime. The orientation of derived nodal planes and six fault segments depicted from the refined earthquake distribution collectively define the overall geometrical characteristics of the RSS. Mohr-Coulomb failure analysis further suggests a cumulative stress perturbation of up to 10.0 MPa. The dimension of RSS could be important in the assessment of the overall seismic hazard due to fluid injections.

1. Introduction

It is generally accepted that randomly distributed small fault segments would eventually evolve into a mature strike-slip fault system, when the source region is subjected to a deviatoric stress field under transpressional or transtensional tectonics over a significant period of time (Riedel, 1929; Tchalenko, 1968). In a simple shear stress regime, Riedel shear structures (RSS) are frequently observed during the embryonic stage of strike-slip fault development. Typical RSS often involve a set of conjugated fault segments that interact with each other prior to the growth of a through-going fault, i.e., the principal deformation zone (PDZ) (Riedel, 1929; Tchalenko, 1968; Katz et al., 2004). As shown in Fig.1, the PDZ usually orients 45±5° to the principal shear stress regardless of the local lithology and regional stress condition, (Bartlett et al., 1981). The right lateral shear structures R and P are synthetic to the sense of shear slip along the PDZ, whereas the left lateral shear structure R' is antithetic. Ideally, structures R and P are symmetric to the PDZ; structures R and R' are conjugated. They inclined respectively $\varphi/2$ (R), $-\varphi/2$ (P) and $90°-\varphi/2$ (R') with respect to the strike of the PDZ, where φ is related to the internal friction of the rock matrix (defined as the peak angle of shearing resistance, Tchalenko, 1970; Davis et al., 2000; Ahlgren, 2001).

One important feature of RSS is that various rupture modes may exist simultaneously during the process, as long as they are compatible with the background stress regime (Sylvester, 1988). Specifically, based on an idealized Riedel shear model, thrust-faulting events could occur within the compressional zone where S_{Hmax} coincides with the maximum compressive principal stress (σ_1), whereas normal-faulting events occur within the extensional zone where the minimum horizontal stress (S_{Hmin}) corresponds to the minimum compressive principal stress (σ_3). For strike-slip events, they tend to occur along several shear structures in response to the stress regime where S_{Hmax} and S_{Hmin} are respectively σ_1 and σ_3 (Fig. 1; Anderson, 1951). RSS of different sizes are widely documented within different rock types and geologic settings, including those observed in the macro-scale (e.g., Katz et al., 2004; Scholz et al., 2010; Hsu et al., 2019), meso-scale (e.g., Davis et al., 2000; Ahlgren, 2001), micro-scale (e.g., Arboleya and Engelder, 1995) and laboratory experiments (e.g., Tchalenko, 1970).

In a tectonic environment, RSS could be identified through outcrops of fault structures or high-resolution subsurface structural imaging (e.g., Luo et al., 2020; Peirce et al., 2014). Earthquake geologists conduct surveys following moderate-to-large earthquakes to investigate the co-seismic surface rupture distribution along with corresponding landslides. By comparing with RSS, it is possible to illuminate the nearby seismogenic faults and their geometrical characteristics, and to accordingly predict focal mechanisms of future events (e.g., Luo et al., 2020; Angelier et al., 2004; Rao et al., 2011). In western Canada, RSS have been widely observed in northeastern British Columbia, Alberta, Saskatchewan and Northwest Territories (e.g., Peirce et al., 2014; Eccles et al., 2002; Hillacre et al., 2017; Bostock and van Breemen, 1992). Beyond being of interest to economic geology, such observations also help us understand the tectonic stress regime and the stage of structure development. Meanwhile, it is well known that anthropogenic earthquakes can also be big, comparable to damaging natural/tectonic events (e.g., Durrheim et al., 2006; Ellsworth, 2013), yet the structural development of these large induced events remains poorly understood.

During the past decades, the growing number of injection-induced earthquakes (IIEs) has become a main concern in many parts of the world (Ellsworth, 2013; Atkinson et al., 2016; Lei et al., 2020). The drastically rising number of IIEs in central US and western Canada demonstrate that long-term subsurface injections would eventually elevate the seismogenic capability in local areas. Considerable efforts have been made to decipher the seismogenic processes of IIEs (e.g., Hough and Page, 2015; Schultz et al., 2020; Wang et al., 2022), especially the scenarios of relatively large events on reactivated pre-existing faults (Keranen, 2013; Eyre et al., 2019; Wang et al., 2021; Lei et al., 2020). For example, as per in-situ stress measurements conducted near the Duvernay unconventional reservoirs (one of the most active injection areas in western Canada), fluid injections lead to a high level of ambient fluid pressure sufficient to reactivate pre-existing faults that are hydraulically connected to injection wells (Shen et al., 2019a, 2019b). However, the possible impact of long-term fluid injection to the structural development as manifested by these large induced events is still an open question.

In this paper, we present a case study conducted near the Musreau Lake area, central-west Alberta, Canada. As shown in Fig. 2a, this area is inside the Western Canada Sedimentary Basin (WCSB), which contains one of the largest reserves of petroleum and natural gas in the world. Specifically, it is located immediately west of the Fox Creek area, one of most active induced seismicity zones in the WCSB during the past decade (e.g., Bao and Eaton, 2016; Eyre et al., 2019; Schultz et al., 2020). The geological setting in our study area is characterized by the thin-skinned, NW–SE-trending, fold-and-thrust belt of the Rocky Mountain foreland basin, where the oil and gas resources within the Duverney shale formation have spurred a huge interest of industrial exploitations (Shen et al., 2021). Fluid injections in the study area have been actively conducted for 25 years, yet no earthquake was reported until very recently (Yu et al, 2021). The long-term seismic quiescence is previously attributed to the unfavorable orientation of the pre-existing structures and/or the limited level of stress perturbations caused by fluid injections (Schultz et al., 2016). Although fault structures in the study area have not been investigated as thoroughly as in the nearby Fox Creek area (e.g., Chopra et al., 2017; Corlett et al., 2018; Weir et al., 2018), it has been suggested that they correspond to widespread basement-rooted faults distributed along the Devonian reef margin (Schultz et al. 2016).

Until recently, a series of 187 small- and moderate-sized earthquakes (local magnitude, M_L, ranging 1.3–3.9) occurred between January 2018 and July 2021. We denote them as the Musreau Lake sequence (Figs. 2b-c; Yu et al., 2021). These anthropogenically accelerated earthquakes in the area with historical quiescence of background seismicity may provide a unique opportunity to investigate the potential role of fluid injection in the development process of a fault system. In the following, we show consistent observations, including fault traces delineated from local seismicity, earthquake focal mechanisms, and rupture directivity of earthquake sources, to document for the first time how long-term, large-scale fluid injections affect the local seismotectonic setting, facilitate the corresponding seismogenic process, and expedite the development of RSS.

2. Data and Method

Our analysis is based on the earthquake catalog compiled by the Alberta Geological Survey (AGS) for the study area between 2018/01/01 and 2021/07/16 with a total of 187 events (Fig. 2b; Table S1). We collect event waveforms recorded by regional seismograph stations with the epicentral distance less than 250 km. The station distribution used in this study is shown in Fig. 2a.

First, we perform double-difference relocation to enhance the earthquake locations (Waldhauser, 2001; Waldhauser and Ellsworth, 2000; Yu et al., 2016). The relocation is constrained by travel time differences of P- and S-phase arrivals, which are obtained from both manual picking and waveform cross-correlation (see more details in Text S1). Number of available event pairs and details of parameter settings used in the relocation process are listed in Table S2. The CRUST 1.0 velocity model is used to calculate the theoretical travel times (Laske et al., 2013; Table S3). We also try another local velocity model developed by Eaton et al. (2018) for relocation of induced seismicity in the Fox Creek area, Alberta. The result has a higher value of travel time residual but the seismicity distribution appears to be consistent.

A total of 180 out of 187 events are successfully relocated, and the scattering of epicenters is significantly reduced (Fig. 2b). It is important to point out that (1) the relocation using only stations at regional epicentral distance provides more robust constraint on epicenter locations than focal depths, and (2) the absolute epicenter locations are not as accurate as relative locations since the double-difference method relies on the travel time differences, especially along the NE–SW direction where azimuthal coverage is relatively poor (Fig. 2a). We obtain the relocation uncertainty through a bootstrap random replacement error estimation based on 1000 trials (Text S1; Waldhauser and Ellsworth, 2000; Yu et al., 2016, 2019). Among the 180 successfully relocated earthquakes, 18 events have epicentral errors larger than 1 km or vertical errors larger than 2 km, therefore, are excluded from further analysis.

Next, we use the open-source software *Grond* (Heimann et al., 2018) to estimate the moment tensor solutions of earthquakes with magnitude larger than 2. *Grond* performs a Bayesian bootstrap-based probabilistic joint inversion to find the optimal moment tensor and seismic moment as well as their model uncertainties by fitting respectively the shape of envelope, frequency and time domains of each waveform record (see more details in Text S2). Given that the isotropic component is negligible for IIEs in the Fox Creek area (< 4%; Wang et al., 2016), here we only resolve deviatoric moment-tensor solutions. That is, we only constrain the compensated linear vector dipole (CLVD) and the double-couple (DC) component under the assumption that the isotropic component is zero. A representative example of moment-tensor inversion is shown in Fig. S1.

3. Result

During the initial seismicity surge in 2019, the distribution of epicenters was highly correlated with the wastewater disposal (WD) activities in the area (Yu et al., 2021). Local seismicity remains active since then, during which more seismogenic structures may have been re-activated. To depict them explicitly, we look into the spatiotemporal distribution of earthquakes, their focal mechanisms, and the stress state along the hosting faults.

3.1 Spatiotemporal distribution of IIEs

We first illustrate the temporal correlation between WD injections and the local earthquake pattern in the period of 2019–2021. As shown in Fig. 2c, the seismic response is highly related to injecting volumes at three WD wells (#486871, #488015, and #460875). The number of earthquakes jumped up either in the same months when all three wells increased injecting volumes (e.g., Aug 2019: 4 events, Dec 2019: 25 events, Mar 2021: 11 events, and May 2021: 39 events), or in the following months when the injected volume increased sharply at wells #485871 and #488015 but decreased slightly at well #460875 (e.g., May 2019: 5 events, and Oct 2020: 21 events). Moreover, the number of induced events is not linearly proportional to the injected volume. Rather, it is a function of both injected volume and time. For example, no earthquake was induced during Aug 2018, Jan 2019, and Mar 2019 when the monthly injected volumes increased considerably (i.e., by an average of 8000 m^3, 19000 m^3, 16000 m^3, respectively, Fig. 2c). In contrast, a surge of seismicity with 39 events in total was observed in May 2021 when the amount of injected volume was increased by only 3400 m^3. Another 11 events were induced in the following month of June 2021.

Spatially, the enhanced relocation result shows that all events clustered near the injection wells (Fig. 2b). All WD wells target aquifers beneath the Winterburn group. Specifically, the injection depth of well #460875 is 4.4 km, i.e., about 0.4 km deeper than the other wells. Based on the sequence of Devonian stratigraphic and hydrostratigraphic layers, Yu et al. (2021) infers that well #460875 targets the deeper Middle-Upper Devonian aquifer system, while the other wells target the shallower Upper Devonian aquifer system. The two aquifer systems are separated by the Woodbend aquitard. Focal depth analysis further suggests that induced events clustered at injection depths. We refer readers to Yu et al. (2021) for more details about injection operations, and the corresponding earthquake triggering hypotheses.

To reveal more detailed geometrical features of the seismicity distribution, we present the relocated events chronologically in Figs. 3a-c. In 2019, active injection-related seismicity began to appear in the historically seismically quiet area. The overall seismic pattern consists of three clusters located ~1 km northward to well #485871, ~1 km northwest of well #488015 and proximal to well #460875, respectively (Fig. 3a). As we zoom-in, the latter two clusters respectively delineate one and two small fault segments, denoted as faults F1, F2 and F3 in Fig. 3d. Here we require at least ten earthquakes to perform a linear least-square regression. The three faults have similar length of ~2 km and orient approximately along the NNE–SSW direction (strike 24°, 19° and 17°, respectively). In 2020, seismicity near fault F1 was still active (Fig. 3b). The subsequent earthquakes highlight another structure that is sub-parallel to fault F1 (striking 12° vs 24°), denoted as fault F4 in Fig. 3d. Furthermore, later earthquakes in September–December 2020 diffusely distributed in the area between well #488015 and #460875 (Fig. 3b). Among them, two subgroups are proximal to well #460875; the one on the west side was newly activated and the other one on the east side is compatible with fault F2 (Fig. 3d). In 2021, seismicity continued to occur near the three wells. Specifically, the subgroup to the west of well #460875 grew rapidly, and expanded to form an "L" shape, which could be delineated into the NNW–SSE-striking fault F5 and the E–W-striking fault F6 (Fig. 3c-d). The two faults are connected to faults F1–F4. The lengths of faults F5 and F6 are about twice of that of faults F1–F4 (Fig. 3d). For each fault, Table S4 lists the number of events used in the linear fitting process and the averaged distance between events and the fitted fault (as a parameter of fitting performance). Given the generally abundant data (10–65 events per structure) and small event-to-fault distances (0.2–0.3 km), the linear fitting results are deemed robust. Moreover, the spatial distribution of local seismicity seems to suggest more fault structures being reactivated. We do not attempt to image them as we require at least ten earthquakes to delineate a fault structure. Nevertheless, these relatively less well-defined structures are more or less parallel to F1–F4.

3.2 Fault orientations and earthquake focal mechanisms

In total, we resolved 31 deviatoric moment-tensor solutions after quality control (Text S2). Table S1 lists full details of event parameters, including origin time, source location and focal mechanism. On average, our moment-tensor solutions have a CLVD component of 16±12%, comparable to the value of 23±17% reported by Wang et al. (2016) for the 2015 Mw3.9 earthquake in Fox Creek, Alberta. The considerable CLVD component of IIEs could be associated with the fluid-driven opening/closing process of cracks (Frohlich, 1994), or the geometric complexity of the faults (e.g., Liu and Zahradník, 2020; Yang et al., 2021), but will not be discussed further as it is beyond the scope of this study. Here we only use the more dominant DC component to infer the rupture mode.

In Fig. 3, we also plot the DC component of the 31 moment-tensor solutions. Over the whole study period, the most notable source feature is the co-existence of various rupture types in the study area. Specifically, fourteen events show oblique strike-slip mechanisms (events #23, #24, #32, #45, #62, #146, #147, #149, #157, #163, #178, #179, #184, and #185); nine events manifest as thrust faulting (#14, #25, #36, #42,

#94, #112, #161, #166, and #175); and eight are normal-faulting events (#26, #46, #95, #96, #111, #127, #153, and #156).

Despite the diverse faulting types, 27 out of the 31 focal mechanisms are compatible with a NE–SW compressional stress regime. The remaining 4 focal mechanisms (events #94, #111, #153, #163) manifest a conjugate stress regime (i.e., NW–SE compression), which, according to our further quality tests (see more details in Text S3; Fig. S2), is unlikely to be an inversion artifact. We will further discuss the rupture complexity of these four events in Section 4.3.

The orientation of individual faults outlined by seismicity are generally comparable to the strikes of resolved nodal planes. For examples, when comparing focal mechanisms of twelve $M_L \geq 3$ earthquakes with delineated faults F1–F6 (Fig. 3d), one nodal plane of event #184 is parallel to fault F1 (207° vs 24°), so is event #32 to fault F2 (197° vs 19°), event #178 to F4 (12° vs 12°), event #14 to F5 (342° vs 340°) and event #146 to F6 (76° vs 80°). However, we notice an interesting pattern for fault F6 (strike = 80º). There are four focal mechanisms that can be associated with this fault (events #24, #147, #149, and #157). All of them appear to have one nodal plane oriented ~15º clockwise from the strike of fault F6 (Fig. 3d; ~95° vs 80°). The two remaining strike-slip events (#62 and #185) also have one of their nodal planes striking approximately 95°.

3.3 Emerging Riedel shear structures (RSS)

The facts that (1) the vast majority of focal mechanisms with diverse faulting types are consistent with one regional stress regime and (2) six out of the twelve $M_L \geq 3$ oblique strike-slip events consistently have one nodal plane deviated 15º from the strike of fault F6, lead us to hypothesize that the overall seismic pattern since 2018 in the study area is a manifestation of emerging RSS.

Next, we infer the geometry of RSS based on the strikes of resolved fault planes. We assume that all induced earthquakes here occurred along pre-existing faults. That is, sub-structures of RSS are reactivated, rather than newly created, by the fluid injections. Therefore, the internal friction angle (φ) should be the same as the frictional coefficient. In our case, since we have limited constraint on the value of μ in our study area (Shen et al., 2019b), we simply assume it with a typical value of 0.6 for the host rocks mainly composed of sandstone, siltstone, and limestone

(Buschkuehle and Michael, 2006). The equivalent angle of friction φ is 30° (Barton and Choubey, 1977). We prescribe a model of RSS using the azimuth of PDZ, since other sub-structures can be expressed with the PDZ and φ (Fig. 1). Specifically, we conduct a grid search to find the optimal orientation of PDZ, in the range of 20°–70° (i.e., 45°±25°) deviated from S_{Hmax}, with an increment of 1° (Fig. S3).We set the azimuth of S_{Hmax} as N38°E, predicted from available borehole breakout measurements (Shen et al., 2019a). The solution with the lowest root-mean-square (RMS) error is considered best-fitting (in our case the strike of PDZ is N94°E). An alternative RSS model with a nearly N–S striking PDZ (N12°W) might also be plausible, though with a relatively higher RMS error. Detailed evaluations between the two RSS models are available in the following Section 4.2, based on which we propose that the model with E–W striking PDZ is more favored. Further analysis and discussion will be mainly focused on the E–W striking model.

In Fig. 4, we project focal mechanisms to the E–W striking model of RSS. Seven strike-slip events are considered to rupture along the PDZ, namely, #24, #45, #62, #147, #149, #157, and #185. The corresponding strike of structures R and R' are respectively 79° and 19°. Three resolved strike-slip events likely ruptured along these two structures, namely, #146 along structure R and #32 and #178 along structure R'. Four other strike-slip events (#23, #163, #179 and #184) may have ruptured along structure P, which has a strike of 109°. Six normal events (#26, #46, #95, #96, #127, and #156) are associated with tension fractures (in green areas), whereas eight thrust events (#14, #25, #36, #42, #112, #161, #166, and #175) likely occurred along the compressional textures (in pink areas).

Furthermore, faults outlined by the epicenter distribution are consistent with the orientation of structures R and R'. Specifically, faults F1–F4 are roughly parallel to R' and fault F6 aligns with R. Fault F5 most likely manifests one of the compressional structures that host thrust-faulting events.

3.4 Geomechanical analysis of different earthquake rupture types

In order to evaluate the cumulative stress perturbations caused by long-term fluid injection, we conduct a retrospective Mohr-Coulomb failure analysis upon the resolved earthquake focal mechanisms. We first describe the local stress state near focal depths. According to the precise focal depths constrained by the timing of local and regional depth phases, Yu et al. (2021) suggest that most earthquakes cluster near the injection depths of ~4 km. The average focal depth differences of the three faulting types are all <1 km (Table S1), which is within the depth uncertainty of up to 2 km. Therefore, here we simplify the vertical distribution by assuming that all the events occurred near the 4-km depth. Next, we look into the principal stresses at the 4-km depth. Shen et al. (2019a) provides a 3D predictive model of stress state distribution in a 150 km-by-150 km area centred near Fox Creek, which encompasses our study area along its west boarder. The model is developed by kriging of borehole observations and validated by focal mechanisms. Based on their results, the principal stresses S_{Hmax}, S_V (the vertical stress) and S_{Hmin}, at the 4-km depth in our study area (centered at -118.5°E, 54.5°N) would be, respectively, 110.41 MPa (with values ranging from 96.66 to 140.08 MPa), 94.57 ± 3.66 MPa, and 86.49 ± 3.46 MPa; and the pore pressure (P_p) is 76.87 ± 3.46 MPa. The comparable values of S_{Hmin} and P_p suggest a state of considerable overpressure. We use the center value of the three principal stresses, and assume P_p to be 74.87 MPa to determine the critical stress state (i.e., the Mohr circle intercepts the failure criteria). Specifically, S_1 (i.e., S_{Hmax} - P_p), S_2 (i.e., S_V - P_p), and S_3 (i.e., S_{Hmin} - P_p) are 35.5, 19.7, and 11.6 MPa, respectively (Fig. 5). Although a direct measurement of P_p in our study area is unavailable, the close-to-failure stress state along the preferred orientation seems to suggest that the adopted P_p value is reasonable.

Next, we calculate the corresponding normal and shear stresses along the resolved nodal planes (see more details in Text S4; Fig. S4). The Coulomb failure stress change (ΔCFS) combines effects from normal stress change ($\Delta\sigma_n$), shear stresses change ($\Delta\tau$) and pore pressure change (ΔP_p), defined as $\Delta CFS = \Delta\tau + \mu(\Delta\sigma_n - \Delta P_p)$, where μ is the frictional coefficient (King et al., 1994). As shown in Fig. 5, the amount of stress perturbations (ΔCFS) required for seismic rupture can be obtained by measuring the distance to the failure criteria. We assume each strike-slip event ruptures along the nodal plane approximately parallel to the sub-structures of the inferred RSS model (Fig. 4). For normal or thrust events, we calculate the stress state along both nodal planes, and consider the one with smaller ΔCFS as the favored rupture plane.

As shown in Fig. 5, the inferred ΔCFS varies from 0.3 MPa to 10.0 MPa. Among the three different faulting types, the mode of thrust faulting is most prone to seismic failure, followed by normal faulting. Strike-slip faulting, in general, requires the largest stress perturbations. Specifically, ΔCFS of the thrust-faulting events ranges between 0.3 and 0.8 MPa with an average of 0.5 MPa. For normal-faulting events, it ranges between 2.2 and 3.9 MPa, averaged 3.1 MPa. For strike-slip events, the range and mean value are 0.8–10.0 and 5.9 MPa, respectively. It is worth noting that the ΔCFS values of strike-slip events with $M_L \geq 3$ show no systematic difference from that of smaller events, suggesting that larger earthquakes do not exclusively occur on mature faults.

4 Discussion and Implications

4.1 Active development of RSS driven by long-term injections

Conventionally, RSS can be inferred from the surface rupture distribution after a major earthquake (e.g., Kato et al 2020; Luo et al., 2020). This study is probably the first to use RSS to explain a combination of many individual earthquakes in an area of active fluid injections. The reason that we can do this is because these earthquakes occur very closely in time (on a geological time scale), so that they can be viewed as belonging to the same event sequence. In contrast to naturally developed RSS, however, this "event sequence" is most likely the result of long-term WD injection.

Observations about the dramatic increase of local seismicity in the past few years (Fig. 2c), the co-existence of various faulting types on seismogenic structures with specific orientations (Fig. 4), and consistent fault segments highlighted by epicenters (Fig. 3d-e) collectively suggest that RSS are probably actively developing. According to the Mohr-Coulomb failure analysis, long-term injections probably have increased the ΔCFS by as much as 10.0 MPa, bringing the local structures very close to the critically stressed state (Fig. 5; Lund Snee and Zoback, 2016). Consequently, as the injection continues, the area’s seismic response became more sensitive to the total volume of injected fluids (Fig. 2c).

The developing process of RSS often initiates from low levels of cumulative displacement. Under the progressively shear stress loading, the structure R usually slips first, with or without its conjugate shear structure (i.e., the R’) being established. The process is then followed by slips along the structure P, and eventually the PDZ forms. Regarding our case, strike-slip events along structures R, R’, P and PDZ occurred almost synchronously. Among them, structures R and R’ (respectively corresponding to faults F6 and F1–F4, Fig. 3d-e) seem to host the largest number of earthquakes.

Overall, long-term WD injection in this area not only leads to the elevated local seismicity rate (Atkinson et al., 2020; Schultz et al., 2020), but also significantly expedites the spatial and temporal development of local RSS near the injection wells. It probably has played a determinant role in promoting RSS to a more mature state.

4.2 An alternative model of RSS

Since each double-couple solution has a pair of conjugate nodal planes, it is theoretically possible to obtain an alternative model of RSS with the mainly N–S-striking structures. The PDZ azimuth of the preferred N–S striking model is N12°W (Fig. S3), and corresponding azimuths of shear structures R, R' and P would be respectively N3°E, N63°E, and N27°W (Fig. S5). Next, we conduct a series of comparisons to evaluate the alternative N–S striking model and the E–W striking model.

Regarding the fitting performance, the E–W striking model has an RMS value ~32% smaller than that of the N–S model (4.0° vs 5.3°; Fig. S3). When we compare focal mechanisms with the two RSS models, we find that both models can explain the normal- and thrust-faulting events well, whereas the E–W model performs better in explaining the strike-slip events. Namely, normal-faulting events ruptured along tensile fractures whereas thrust-faulting events occurred within the compressional quadrants (Fig. 5, Fig. S5a). In the E–W striking model, all sub-structures (i.e., PDZ, R, R' and P) are manifested by corresponding strike-slip earthquakes with major events occurring along PDZ (Fig. 5). Furthermore, all strike slip events can be explained by the individual sub-structures of RSS. In the N–S striking model, however, only R and PDZ structures are reactivated by strike slip events, and four oblique strike-slip events are inconsistent with any of the RSS sub-structures (Fig. S5a). Another important difference is that all fitted faults agrees with the E–W striking model, as R' corresponds to faults F1–F4, R to F6, and F5 would host thrust ruptures. In contrast, the N–S striking model cannot justify most of the fitted faults, only that F5 is compatible with structure P.

Li et al. (2021) studied a total of 48 earthquakes from the same sequence, but for a shorter period between January 2018 and March 2020. They suggest that the sequence occurred along an approximately NNW–SSE-striking structure, by considering (a) the three clusters during the emerging stage (Fig. 3a) appear to align in the NNW–SSE direction, (b) the consistently parallel orientation of nodal planes, plus (c) the widespread NW–SE-striking fault structures in the foreland basin area. However, the inference of a NNW–SSE-striking fault connecting three earthquake clusters could be erroneously drawn due to several factors. The foremost consideration is that the three clusters should be spatially correlated with the location of injection wells, which happened to align approximately NW–SE. The much fewer number of events analyzed by Li et al. (2021) also means a lack of sufficient spatial resolution to delineate detailed structures as shown in Fig. 3d-e. Moreover, their fault plane solutions were determined from the polarities and amplitudes of P and S phases that can be severely contaminated by background noise, especially for signals of smaller events at regional distances. The poor station coverage in the southwest quadrant of the source area further contributes to the uncertainty. These drawbacks become evident as the fault plane solution of the largest M_L3.9 event has a relatively poor quality grade of "D" on a scale of A–E (Hardebeck and Shearer, 2008).

However, when comparing the two models with previous knowledge in the western Alberta region, the N–S striking model seems to be more favored than the E–W striking model. Firstly, the N–S striking model is compatible with the local S_{Hmax} predicted from borehole measurements (N38°E; Shen et al, 2019a), as the angle between S_{Hmax} and PDZ of the N–S model (N12°W) is 50° but increases slightly to 56º in the E–W striking model (PDZ in N94°E). Correspondingly, the inferred ΔCFS along fault planes of strike-slip events parallel to the N–S-striking model varies from 1.6 MPa to 6.7 MPa, with a mean value of 4.2 MPa (Fig. S5b), which is about 1.7 MPa closer to failure than those with the E–W model (5.9 MPa). Furthermore, high resolution seismic reflection survey in the nearby Fox creek area show that N–S striking planes are more dominant, and induced events there appear to occur along these planes (e.g., Chopra et al., 2017, Weir et al., 2019).

Despite the controversy, we consider the E–W striking model a valid alternative because (1) a small deviation (~5°–10° in this case, Fig. S3) in the direction of S_{Hmax} from borehole breakouts and focal mechanisms is acceptable, as the latter is an indirect proxy with a comparable uncertainty, (2) the PDZ orientation (N94°E) is compatible with the regional S_{Hmax} (N43°E; Fig. S3), (3) it is possible for the long-term fluid injection to cause a ΔCFS up to 10 MPa (e.g., Shen et al., 2019a), especially when structures hydraulically connected to the fractured zone are reactivated to allow more effective fluid migration, and (4) RSS with PDZ striking E–W are suggested by high-resolution magnetic surveys in local areas within the WCSB, where a similar NE–SW compressional stress regime is prevailing (e.g., Peirce et al., 2014; Hillacre et al., 2017).

A summary of aforementioned comparisons is provided in Table 1. Overall, the E–W striking model can better justify the observed earthquake sequence, while the N–S one is more consistent with previous knowledge in the western Alberta region. To consider all the pros and cons of the two models, we cautiously propose that the E–W striking model is more favored here. Regardless the choice, the preference of either model will not influence the highlight of this study, that is, to document a clear case of local fault system development/reactivation expedited by long-term fluid injections.

To further investigate the geometrical configuration of seismogenic structures associated with the observed seismicity, we conduct rupture directivity analysis for all events in the sequence. Five of them have sufficient data quality to give meaningful results (more details in Text S5). As shown in Fig. S6, all the resolved rupture propagations are consistent with the orientation of the respective focal mechanisms, including one strike-slip event (#32), one thrust event (#175) and three normal-faulting events (#95, #96, #156). The consistency between rupture directivity and focal mechanism would strengthen our inference of the co-existence of various faulting types, and thus the proposed RSS model. In the nearby Fox Creek area, Holmgren et al. (2019) also report a mixture of at least 3 different rupture azimuths for small and moderate-sized events (M_L 2.3–4.4), including N–S, NE–SW parallel to the regional S_{Hmax}, and NW–SE parallel to S_{Hmin}, which could be compatible with the proposed RSS model as well (Fig. 4).

Nevertheless, we note that the lineup of earthquakes with similar focal mechanisms in neither of the two RSS models (Fig. 4 or Fig. S5) would faithfully follow the distribution of epicenters shown in Fig. 3. For examples, the epicenters of normal- and thrust-faulting events do not necessarily scatter between the major strike-slip structures. One possible explanation is that there may be more than one Riedel shear zone concurrently in development due to injections at multiple wells. Epicentral location error can also contribute, at least partially, to this mismatch.

4.3 Events with inconsistent sense of slip

We observed four events whose focal mechanisms indicate a conjugate stress regime (P-axis rotates by 90°) to the local stress field, i.e., events #94, #111, #153 and #163; Fig. 4). Similar observations have been reported for micro-sized earthquakes (magnitude ranging between -3 and 2) during hydraulic fracturing operations (e.g., Eyre and Van de Baan, 2018; Chambers et al., 2017; Staněk and Eisner, 2013). One of the proposed interpretations might be applicable to our case, as injected fluid is capable of opening fractures in close proximity of the injection wells. Such volumetric change would further cause dislocations along the nearby weak planes, along which the sense of slip only depends on their relative locations to the fracture, thus allowing opposite shear motion to occur (Eyre and Van de Baan, 2018; Staněk and Eisner, 2013).

A viable explanation is that these four back-propagating ruptures manifest local stress adjustments during the period of intense seismicity. Similar examples of reversed polarity were documented in the Changning block, Sichuan, China between 2014 and 2019, when the peal level of induced seismicity was observed (Lei et al., 2019).

4.4 Applications to other areas in the WCSB with large-scale injections

Although this is a case study focusing on a local area in Alberta, our inference of the active development of RSS could be applicable to other intraplate settings where large-scale injections also expedite the evolving process of local and regional fault systems. Specifically, the regional geology in northeastern BC and western Alberta is mainly featured by the Rocky Mountain foreland basin with the underlying Precambrian basement where the orientation of pre-existing shear zones/faults is mainly in the NW–SE direction (Ross et al., 1994). Under the modern NE–SW compressional stress regime, the expected mode of rupture at shallow depths would be thrust. It requires extra stress loading to initiate strike-slip faulting, of which the preferred orientation is either E–W or N–S (Figs. 5, S5b). Thus, a change of the faulting pattern from co-existence of thrust and strike-slip events to purely strike-slip might manifest the development of a young shear fault system (i.e., RSS).

In addition to our study area, we notice a similar change of faulting pattern in the Fox Creek area, another induced seismicity hotspot in the WCSB. In this area, IIEs that occurred before January 2015 show a mixture of normal- and thrust-faulting mechanisms (Eaton and Mahani, 2015; Kao et al., 2012; Zhang et al., 2016), while events occurred afterwards are exclusively strike-slip with nodal planes striking E–W or N–S (Wang et al., 2016; Schultz et al., 2017; Zhang et al., 2019). We speculate that large-scale injection operations in Fox Creek, Alberta, might have also expedited the development of local fault systems.

Another possible case of active development of RSS is in the Dawson Creek area of British Columbia, ~200 km NW of our study area (Fig. 2). Although reliable moment tensor solutions for minor to moderate-sized IIEs in this area are not available until 2017, due to the relatively poor station coverage in this part of Canada, earthquakes before 2014 seem to be purely thrust-faulting (Kao et al., 2018), while during the more recent period of 2017–2020, the portion of thrust-faulting ruptures dropped to only 22% (the remaining 78% are mostly strike-slip events, Roth et al., 2022).The co-existence of different faulting types is also compatible with the limited number of rupture directivity observations in the region (Holmgren et al., 2019).

At last, our case study shows that the spatiotemporal distribution of various faulting types in an anthropogenic environment can provide new insights into the recognition of Riedel shear zones. In particular, long-term injection could efficiently build up the stress level near injection sites to expedite fault development. A possible consequence of this process is the increasing maturity of primary fault segments that may be able to host large earthquakes. For example, the length of seismicity distribution along faults F1–F4 is on the order of 1–2 km, which is comparable to the dimension of RSS reported by post-earthquake measurements from field surveys (e.g., Hsu et al., 2019; Luo et al., 2020) and typical for an M4 earthquake according to the Brune model (Stein and Wysession, 2003). Such an inference is remarkably consistent with the largest event in the sequence (M_L3.9, #24). If we assume the maximum length of the individual Riedel shear zone to be 5–10 km (i.e., across the entire seismicity area), then a throughout rupture in this area could lead to a damaging earthquake with M_L

between 5 and 6. Therefore, it is probably important to consider the overall dimension of local/regional RSS in the assessment of seismic hazard due to IIEs.

5 Conclusion

In this study, we investigate source characteristics of an injection-induced earthquake sequence consisting of 187 events (M_L 1.3–3.9) in western Canada with no historical background seismicity. We first show that the relocated distribution of epicenters delineates six seismogenic faults (F1-F6) ranging from 2 to 5 km in length. Next, we are able to resolve moment-tensor solutions for 31 events, and the results exhibit various types of faulting, including thrust, normal and strike-slip. The vast majority of derived focal mechanisms (27 out of 31) are consistent with the background stress regime where the maximum horizontal stress (S_{Hmax}) is oriented N38°W.

We propose a Riedel shear model to understand the co-existence of various rupture types. Constrained by the orientation of derived nodal planes, the inferred Riedel shear structures (RSS) coincide with the background stress orientation. Specifically, it consists of four primary strike-slip structures respectively striking 19º (R'), 79º (R), 94º (PDZ) and 109º (P). Moreover, the six seismically highlighted fault segments (F1-F6) are parallel to the sub-structures of RSS.

Retrospective Mohr-Coulomb failure analysis further suggests that the cumulative Coulomb stress change (ΔCFS) associated with long-term injection could reach up to 9.1 MPa, which brings faults with different rupture types very close to failure. According to derived nodal planes, thrust faulting is most prone to seismic failure (requires an average ΔCFS of 0.5 MPa), followed by normal faulting (3.1MPa), and strike-slip faulting requires the largest stress perturbations (5.9MPa).

Overall, our study suggests that long-term fluid injection could reactivate and promote RSS near the injection wells to a more mature state, expediting the development of local fault systems. In this context, the dimension of local/regional RSS could be a critical parameter in the assessment of the overall seismic hazard due to fluid injections. Observationally, the clustered distribution of various faulting types in an anthropogenic environment can provide new insights into the recognition of Riedel shear zones.

Acknowledgements

Earthquake catalog is downloaded from the webpage https://ags-aer.maps.arcgis.com/apps/webappviewer/index.html?id=4fbf09ad8bf940a9b3945e9c9ab57c78 Last Access: July 16, 2021.Waveforms from the TransAlta network (FDSN codes TD), Canadian National Seismic Network (FDSN codes CN/PQ and 1E), Regional Alberta Observatory for Earthquake Studies Network (FDSN code RV), and EON-ROSE Network (FDSN network code EO) can be obtained from the Data Management Center of the Incorporated Research Institutions for Seismology (IRIS; https://ds.iris.edu/ds/nodes/dmc/). Raw data from the McGill University Dawson-Septimus Induced Seismicity Study Network (FDSN code XL) can be available at IRIS after a 2-year embargo period. Well locations and operation parameters can be obtained through a subscription to the geoLOGIC database at https://www.geologic.com/. Earthquake waveforms and well information used in this study are available at https://zenodo.org/record/6169096#.YhEzl-7MKys. Open-source software hypoDD and Grond can be respectively downloaded from https://www.ldeo.columbia.edu/~felixw/hypoDD.html and https://pyrocko.org/grond/docs/current/. This paper is NRCan contribution 2022xxxx.

Reference

Anderson, E. M. (1951). The Dynamics of Faulting and Dyke Formation with Applications to Brittan, Edinburgh, Oliver and Boyd. New York City: Hafner Publishing Company.

Angelier, J., Bergerat, F., Bellou, M., Homberg, C. (2004). Co-seismic strike-slip fault displacement determined from push-up structures: the Selsund Fault case, South Iceland. J. Struct. Geol. 26 (4), 709–724. AER. (2015). Subsurface Order No. 2. Calgary, AB: Alberta Energy Regulator. Retrieved from https://aer.ca/documents/orders/subsurface-orders/SO2.pdf

Ahlgren, S.G. (2001). The nucleation and evolution of Riedel shear-zones as deformation bands in porous sandstone. Journal of Structural Geology 23, 1203–1214.

Arboleya, M.L., Engelder, T., 1995. Concentrated slip zones with subsidiary shears: their development on three scales in the Cerro Brass fault zone, Appalachian valley and ridge. Journal of Structural Geology 17, 519–532.

Atkinson, G.M., Eaton, D.W., Ghofrani, H., Walker, D., Cheadle, B., Schultz, R., Shcherbakov, R., Tiampo, K., Gu, J., Harrington, R.M. and Liu, Y. (2016). Hydraulic fracturing and seismicity in the western Canada sedimentary basin. Seismological research letters, 87(3), pp.631-647.

Atkinson, G.M., Eaton, D.W. & Igonin, N (2020). Developments in understanding seismicity triggered by hydraulic fracturing. Nat Rev Earth Environ 1, 264–277. https://doi.org/10.1038/s43017-020-0049-7.

Bartlett, W. L., M. Friedman, and J. M. Logan (1981). Experimental folding and faulting of rocks under confining pressure Part IX. Wrench faults in limestone layers. Tectonophysics, 79, 255-277, doi: 10.1016/0040-1951(81)90116-5.

Barton N, and Choubey V (1977). The shear strength of rock joints in theory and practice. Rock Mech, 10:1–54.

Bostock, H.H. and van Breemen, O. (1992). The timing of emplacement, and distribution of the Sparrow diabase dyke swarm, District of Mackenzie, Northwest Territories. In: Radiometric Age and Isotopic Studies, No. 6. Geological Survey of Canada, Paper 92-2, p. 49-55.

Buschkuehle, B.E. and Michael, K. (2006): Subsurface characterization of acid-gas injection operations in northeastern British Columbia; Alberta Energy and Utilities Board, EUB/AGS Earth Sciences Report 2006-05, 142 p.

Chambers, K., B. Batlai, B. Bialowas, J. Nieto, and D. Baturan (2017). Monitoring in a western Canadian shale play with a sparse surface network: moment tensor analysis implications: URTeC abstract, Austin, Texas, 2670385.

Chopra, S., Sharma, R. K., Ray, A. K., Nemati, H., Morin, R., Schulte, B., & D'Amico, D. (2017). Seismic reservoir characterization of Duvernay shale with quantitative interpretation and induced seismicity considerations—A case study. Interpretation, 5(2), T185-T197.

Clerc, F., R. M. Harrington, Y. Liu, and Y. J. Gu (2016), Stress drop estimates and hypocenter relocations of induced seismicity near Crooked Lake, Alberta, *Geophys. Res. Lett.*, 43, 6942–6951, doi:10.1002/2016GL069800.

Corlett, H., Schultz, R., Branscombe, P., Hauck, T., Haug, K., MacCormack, K., & Shipman, T. (2018). Subsurface faults inferred from reflection seismic, earthquakes, and sedimentological relationships: Implications for induced seismicity in Alberta, Canada. Marine and Petroleum Geology, 93, 135–144. https://doi.org/10.1016/j.marpetgeo.2018.03.008

Davis, G.H., Bump, A.P., Garc´ıa, P.E. & Ahlgren, S.G. (2000). Conjugate Riedel deformation band shear zones, J. Struct. Geol., 22, 169–190.

Durrheim, R.J., Anderson, R.L., Cichowicz, A., Ebrahim-Trolloped, R., Hubert, G., Kijko, A., McGarr, A., Ortlepp, W., van der Merwe, N., 2006. The risks to miners, mines, and the public posed by large seismic events in the gold mining districts of South Africa. In: Proceedings of the Proceedings of the Third International Seminar on Deep and High Stress Mining, 2–4 October 2006, Quebec City, Canada.

Eaton, D. W., Igonin, N., Poulin, A., Weir, R., Zhang, H., Pellegrino, S., & Rodriguez, G. (2018). Induced seismicity characterization during hydraulic‐fracture monitoring with a shallow‐wellbore geophone array and broadband sensors. Seismological Research Letters, 89(5), 1641-1651.

Eaton, D.W. and Mahani, A.B. (2015). Focal mechanisms of some inferred induced earthquakes in Alberta, Canada. Seismological Research Letters, 86(4), pp.1078-1085.

Eccles, D. R. (2002). Structural-emplacement Model for Kimberlitic Diatremes in Northern Alberta. Alberta Energy and Utilities Board.

Ellsworth, W.L. (2013). Injection-induced earthquakes. Science 341, 142–149.

Eyre, T. S. et al (2019). The role of aseismic slip in hydraulic fracturing- induced seismicity. Sci. Adv. 5, eaav7172.

Eyre, T. S., & van der Baan, M. (2018). Microseismic insights into the fracturing behavior of a mature reservoir in the Pembina field, Alberta. Geophysics, 83(5), B289-B303.

Frohlich, C. (1994), Earthquakes with non-double-couple mechanisms, Science, 264(5160), 804–809.

Hardebeck, J. L., and P. M. Shearer (2008). HASH: A FORTRAN Program for Computing Earthquake First-Motion Focal Mechanisms-v1.2-January 31, 2008.

Haskell, N. A. (1964). Total energy and energy spectral density of elastic wave radiation from propagating faults, *Bull. Seismol. Soc. Am.,* 54, no. 6A, 1811–1841.

Heimann, Sebastian; Isken, Marius; Kühn, Daniela; Sudhaus, Henriette; Steinberg, Andreas; Vasyura-Bathke, Hannes; Daout, Simon; Cesca, Simone; Dahm, Torsten

(2018): Grond - A probabilistic earthquake source inversion framework. V. 1.0. GFZ Data Services.https://doi.org/10.5880/GFZ.2.1.2018.003.

Hillacre, S., Ansdell, K., McEwan, B., & McNamara, G. (2017). Structural analysis, paragenesis, and preliminary geochronology of the Arrow uranium deposit, Athabasca Basin, northern Saskatchewan, Canada: Implications for controls on mineralization. In Proceeding of the 14th SGA Biennial Meeting (Vol. 20, No. 23, pp. 743-746).

Holmgren, J.M., Atkinson, G.M. and Ghofrani, H., (2019). Stress drops and directivity of induced earthquakes in the Western Canada Sedimentary Basin. *Bulletin of the Seismological Society of America*, *109*(5), pp.1635-1652.

Hough, S.E., Page, M., 2015. A century of induced earthquakes in Oklahoma? Bull. Seismol. Soc. Am. 105, 2863–2870. http://dx.doi.org/10.1785/0120150109.

Hsu, Y. C., Chang, C. P., Yen, J. Y., Kuo-Chen, H., & Wang, C. C. (2019). Investigating the structure of the Milun Fault from surface ruptures of the 2018 Hualien Earthquake. Terrestrial, Atmospheric & Oceanic Sciences, 30(3).

Kao, H., Shan, S.J., Bent, A., Woodgold, C., Rogers, G., Cassidy, J.F. and Ristau, J. (2012). Regional centroid-moment-tensor analysis for earthquakes in Canada and adjacent regions: An update. Seismological Research Letters, 83(3), pp.505-515.

Kato, A., Sakai, S.I., Matsumoto, S. and Iio, Y. (2021). Conjugate faulting and structural complexity on the young fault system associated with the 2000 Tottori earthquake. Communications Earth & Environment, 2(1), pp.1-9.

Katz, Y., R. Weinberger, and A. Aydin (2004). Geometry and kinematic evolution of Riedel shear structures, Capitol Reef National Park, Utah. J. Struct. Geol., 26, 491-501, doi: 10.1016/j.jsg.2003.08.003.

Keranen, K.M., Savage, H.M., Abers, G.A., Cochran, E.S., 2013. Potentially induced earthquakes in Oklahoma, USA: links between wastewater injection and the 2011 Mw 5.7 earthquake sequence. Geology 41, 699–702.

King, G. C., Stein, R. S., & Lin, J. (1994). Static stress changes and the triggering of earthquakes. Bulletin of the Seismological Society of America, 84(3), 935-953.

Laske, G., G. Masters., Z. Ma, and M. Pasyanos (2013), Update on CRUST1.0 - A 1-degree Global Model of Earth's Crust, *Geophys. Res. Abstracts,* 15, Abstract EGU2013-2658.

Lei, X., Su, J., & Wang, Z. (2020). Growing seismicity in the Sichuan Basin and its association with industrial activities. Science China Earth Sciences, 63(11), 1633-1660.

Lei, X., Wang, Z., & Su, J. (2019). The December 2018 ML 5.7 and January 2019 ML 5.3 earthquakes in South Sichuan basin induced by shale gas hydraulic fracturing. Seismological Research Letters, 90(3), 1099-1110.

Li, T., Gu, Y. J., Wang, J., Wang, R., Yusifbayov, J., Canales, M. R., & Shipman, T. (2021). Earthquakes Induced by Wastewater Disposal near Musreau Lake, Alberta, 2018–2020. *Seismological Research Letters*.

Liu, J., & Zahradník, J. (2020). The 2019 MW 5.7 Changning earthquake, Sichuan Basin, China: A shallow doublet with different faulting styles. Geophysical Research Letters, 47(4), e2019GL085408.

Lund Snee, J.-E., and M. D. Zoback (2016), State of stress in Texas: Implications for induced seismicity, Geophys. Res. Lett., 43, doi:10.1002/2016GL070974.

Luo, J., Evans, S.G., Pei, X., Huang, R., Liu, M. and Dong, X. (2020). Anomalous co-seismic surface effects produced by the 2014 Mw 6.2 Ludian earthquake, Yunnan, China: An example of complex faulting related to Riedel shear structures. Engineering Geology, 266, p.105476.

Park, S., and M. Ishii (2015). Inversion for rupture properties based upon 3-D directivity effect and application to deep earthquakes in the Sea of Okhotsk region, *Geophys. J. Int.* 203, no. 2, 1011–1025.

Peirce, J., Davies, G. R., Goussev, A., Griffith, L., Rhodes, J., & McAuley, R. (2004, January). Structural control of hydrothermal dolomitization in the Keg River and Slave Point formations, Sierra area, NE British Columbia, and analogies with the Ghawar field, Saudi Arabia. In Dolomites—The spectrum: Mechanisms, models, reservoir development: Canadian Society of Petroleum Geologists, Seminar and Core Conference.

Rao, G., A. Lin, B. Yan, D. Jia, X. Wu, and Z. Ren, 2011: Co-seismic Riedel shear structures produced by the 2010 Mw 6.9 Yushu earthquake, central Tibetan Plateau, China. Tectonophysics, 507, 86-94, doi: 10.1016/j.tecto.2011.05.011.

Reiter, K., O. Heidbach, D. Schmitt, K. Haug, M. Ziegler, and I. Moeck (2014), A revised crustal stress orientation database for Canada, Tectonophysics, 636, 111–124, doi:10.1016/j.tecto.2014.08.006.

Riedel, W. (1929). Zur Mechanik Geologischer Brucherscheinungen. Zentral-blatt fur Mineralogie, Geologie und Paleontologie B, 354–368.

Ross, G.M., Broome, J., Miles, W. (1994). Potential Fields and Basement Structure - Western Canada Sedimentary Basin. Geol Atlas West Canada Sediment Basin, Can Soc Pet Geol Alberta Res Counc, 41.

Roth, M. P., Kemna, K. B., Harrington, R. M., & Liu, Y. (2022). Source Properties of Hydraulic-Fracturing-Induced Earthquakes in the Kiskatinaw Area, British Columbia, Canada. *Journal of Geophysical Research: Solid Earth*, *127*(3), e2021JB022750.

Scholz, C. H., R. Ando, and B. E. Shaw (2010). The mechanics of first order splay faulting: The strike-slip case. J. Struct. Geol., 32, 118-126, doi: 10.1016/j.jsg.2009.10.007.

Schultz, R., R. Wang, Y. J. Gu, K. Haug, and G. Atkinson (2017), A seismological overview of the induced earthquakes in the Duvernay play near Fox Creek, Alberta, J. Geophys. Res. Solid Earth, 122, doi:10.1002/2016JB013570.

Schultz, R., Skoumal, R. J., Brudzinski, M. R., Eaton, D., Baptie, B., & Ellsworth, W. (2020). Hydraulic fracturing-induced seismicity. Reviews of Geophysics, 58, e2019RG000695. https://doi.org/10.1029/2019RG000695

Shen, L.W., Schmitt, D. R. and Haug, K. (2018). Measurements of the states of in situ stress for the Duvernay Formation near Fox Creek, west-central Alberta. In: Alberta Energy Regulator/Alberta Geological Survey, AER/AGS Report 97, p. 29.

Shen, L.W., Schmitt, D. R. and Haug, K. (2019a). Quantitative constraints to the complete state of stress from the combined borehole and focal mechanism inversions: Fox Creek, Alberta. Tectonophysics, 764, pp.110-123.

Shen, L. W., Schmitt, D. R., & Schultz, R. (2019b). Frictional stabilities on induced earthquake fault planes at Fox Creek, Alberta: A pore fluid pressure dilemma. Geophysical Research Letters, 46, 8753–8762.

Staněk, F., and L. Eisner (2013). New model explaining inverted source mechanisms of microseismic events induced by hydraulic fracturing, SEG Technical Program Expanded Abstracts, 2201-2205.

Stein, S., & Wysession, M. (2003). An introduction to seismology. Earthquakes, and Earth, 7(9), 10.

Sylvester, A.G. (1988). Strike-slip faults. Geological Society of America Bulletin, 100(11), pp.1666-1703.

Tchalenko, J. S. (1968) The evolution of kink-bands and the development of compression textures in sheared clays. Tectonophysics, 6, 159-174, doi: 10.1016/0040-1951(68)90017-6.

Waldhauser, F., and W. L. Ellsworth (2000). A double-difference earthquake location algorithm: Method and application to the northern Hayward fault, California, *Bulletin of the Seismological Society of America*, 90(6), 1353-1368.

Wang, B., Kao, H., Yu, H., Visser, R., & Venables, S. (2022). Physical factors controlling the diverse seismogenic behavior of fluid injections in Western Canada. *Earth and Planetary Science Letters*, *589*, 117555.

Wang, B., Verdecchia, A., Kao, H., Harrington, R. M., Liu, Y., & Yu, H. (2021). A Study on the Largest Hydraulic Fracturing Induced Earthquake in Canada: Numerical Modeling and Triggering Mechanism. *Bulletin of the Seismological Society of America*, *111*(3), 1392-1404.

Wang, R. (1999), A simple orthonormalization method for stable and efficient computation of Green's functions, *Bull. Seismol. Soc. Am.,* 89(3), 733-741.

Wang, R., Y. J. Gu, R. Schultz, A. Kim, and G. Atkinson (2016), Source analysis of a potential hydraulic-fracturing-induced earthquake near Fox Creek, Alberta, Geophys. Res. Lett., 43, 564–573, doi:10.1002/2015GL066917.

Weir, R., Lawton, D., Lines, L., Eyre, T., & Eaton, D. (2019). Application of structural interpretation and simultaneous inversion to reservoir characterization of the Duvernay Formation, Fox Creek, Alberta, Canada. The Leading Edge, 38(2), 151-160.

Yang, Y. H., Hu, J. C., Chen, Q., Lei, X., Zhao, J., Li, W., ... & Chiu, C. Y. (2021). Shallow slip of blind fault associated with the 2019 M S 6.0 Changning earthquake in fold-and-thrust belt in salt mines of Southeast Sichuan, China. Geophysical Journal International, 224(2), 909-922.

Yu, H., Y. Liu, R. M. Harrington, and M. Lamontagne (2016), Seismicity along St. Lawrence Paleorift Faults Overprinted by a Meteorite Impact Structure in Charlevoix, Québec, Eastern Canada Seismicity along St. Lawrence Paleorift Faults

Overprinted by a Meteorite Impact Structure in Charlevoix, *Bulletin of the Seismological Society of America*, 106(6), pp.2663-2673.

Yu, H., Harrington, R. M., Liu, Y., & Wang, B. (2019). Induced seismicity driven by fluid diffusion revealed by a near-field hydraulic stimulation monitoring array in the Montney Basin, British Columbia. Journal of Geophysical Research: Solid Earth, 124. https://doi.org/10.1029/2018JB017039.

Yu, H., Kao, H., Visser, R., & Wang, B. (2021). From Seismic Quiescence to Surged Activity After Decades of Wastewater Disposal: A Case Study in Central-West Alberta, Canada. *Geophysical Research Letters*, 48(22), e2021GL095074.

Yuan, J., Kao, H., & Yu, J. (2020). Depth-scanning algorithm: Accurate, automatic, and efficient determination of focal depths for local and regional earthquakes. *Journal of Geophysical Research: Solid Earth*, *125*(7), e2020JB019430.

Zhang, H., D. Eaton, G. Li, Y. Liu, and R. M. Harrington (2016), Discriminating induced seismicity from natural earthquakes using moment tensors and source spectra, J. Geophys. Res. Solid Earth, 121, 972–993, doi:10.1002/2015JB012603.

Zhang, H., Eaton, D.W., Rodriguez, G. and Jia, S.Q. (2019). Source-Mechanism Analysis and Stress Inversion for Hydraulic-Fracturing-Induced Event Sequences near Fox Creek, Alberta Source-Mechanism Analysis and Stress Inversion. Bulletin of the Seismological Society of America, 109(2), pp.636-651.

Figures

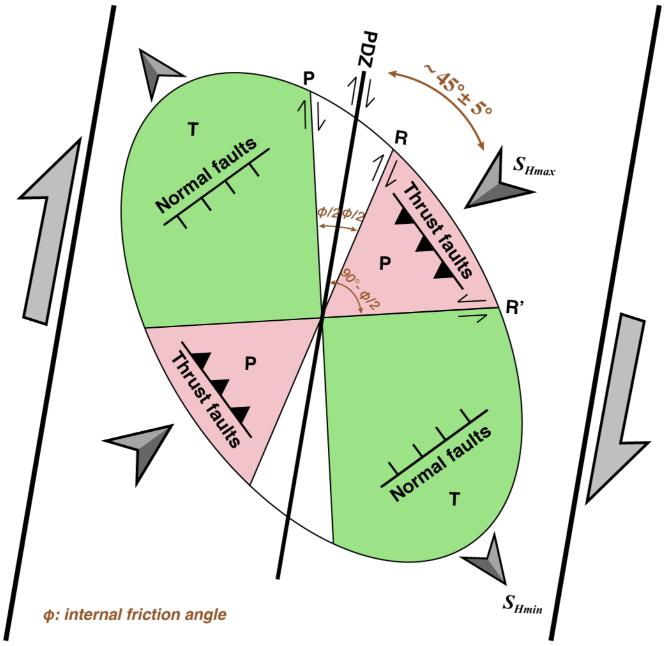

Figure 1. Schematic plot of an ideal Riedel shear zone. PDZ: principal displacement zone. The azimuthal differences between PDZ and S_{Hmax}, shear structures R, R' and P are denoted separately. Pink and green areas are compressional and tensile quadrants, respectively.

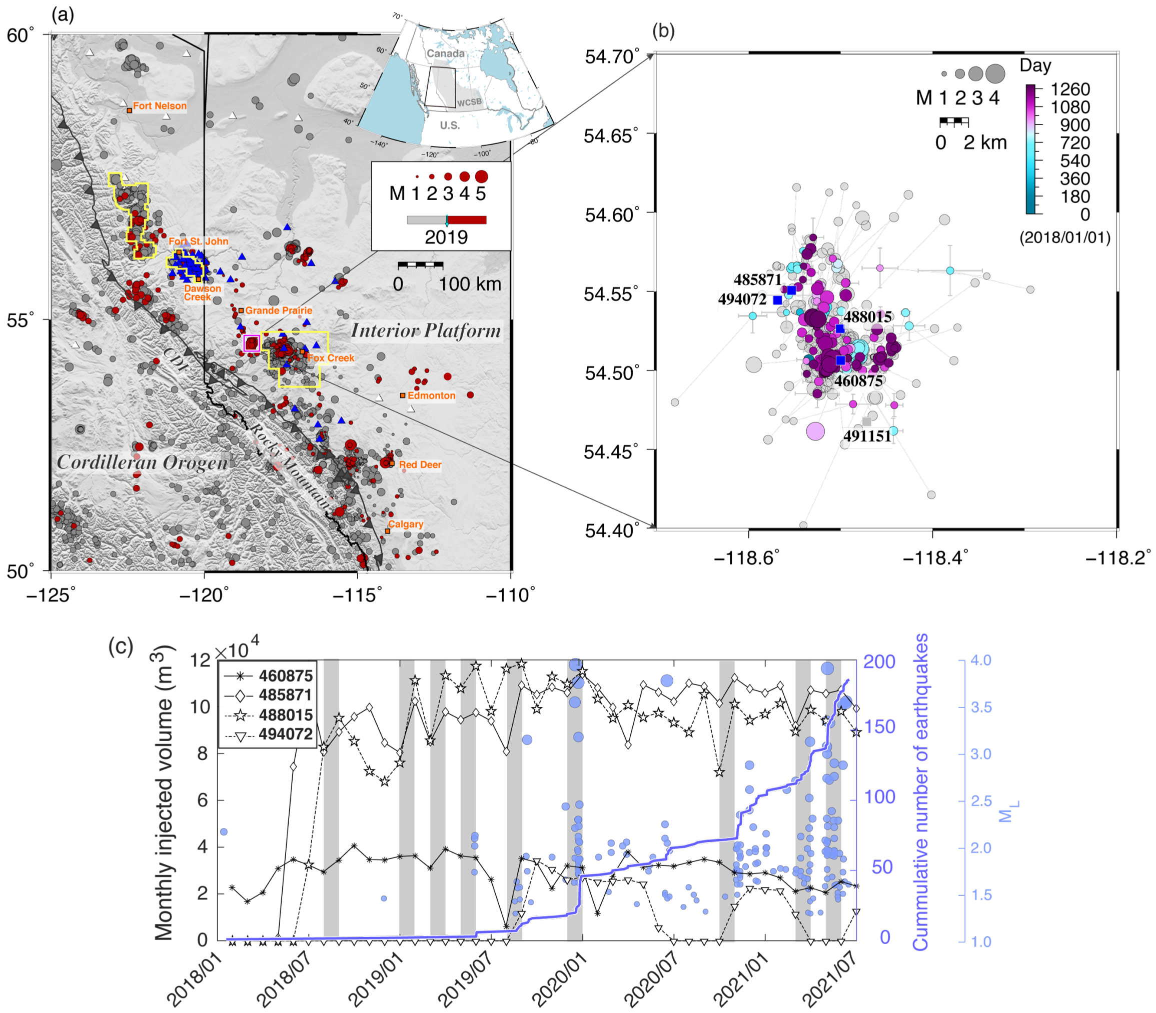

Figure 2. (a) Map of seismicity and seismograph in western Canada. Earthquake catalog (2006/09–2021/07) is reported by Natural Resources Canada and Alberta Geological Survey (AGS). Gray/red circles: 2139/885 earthquakes occurred before and after 2019/01/01, respectively. Circle size scales the magnitude. Blue/open triangles: regional stations being used/unused in this study, depending on the epicenter distance. Areas depicted by yellow lines: enhanced monitoring zones in Alberta and British Columbia. Pink rectangle: study area. Gray curves: Cordilleran deformation front. Inset map shows locations of Western Canada Sedimentary Basin (WCSB, pink area) and the main map (black rectangle). (b) Distribution 180 relocated earthquakes. Dot color and size corresponds to the origin time and magnitude, respectively. Error bars correspond to location uncertainty. Gray dots: initial hypocenter locations. Blue/gray squares: wastewater disposal wells active/suspend during the period of 2018–2021. (c) Temporal comparison between monthly WD injected volumes of different wells (black curves) and induced earthquakes. Gray shaded areas: periods of increasing monthly injected volume at three seismogenic

injection wells #460875, #485871, #488015. Purple curve: cumulative number of earthquakes. Blue dots: earthquake magnitude distribution. Circle size scales with magnitude.

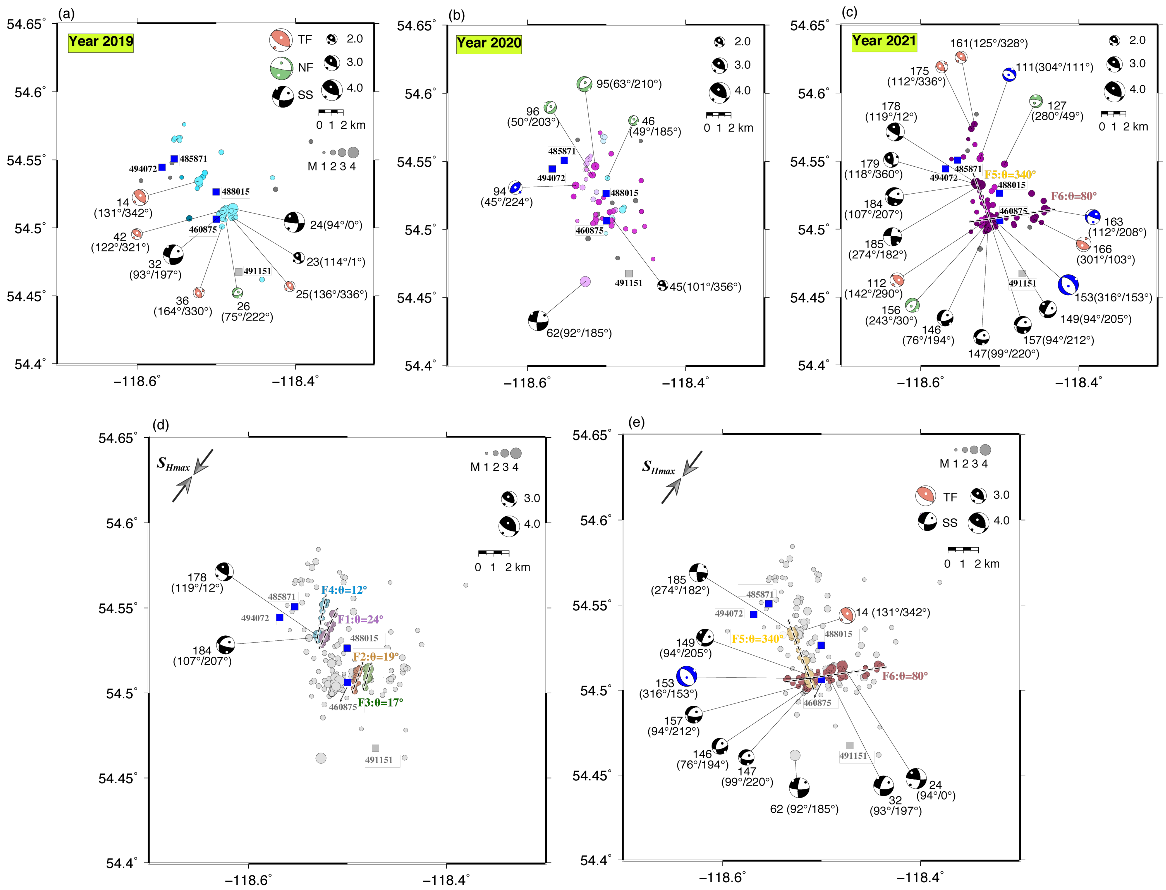

Figure 3. Relocated epicenters and focal mechanisms during (a) Year 2019, (b) Year 2020 and (c) Year 2021. The dots are relocated events shown in Fig. 2b, except that epicentral uncertainty larger than 1 km are shown as gray dots. Black, pink, green beach balls refer to strike slip, thrust, and normal faulting mechanisms, respectively. Blue beach balls are focal mechanisms with opposing stress regime. Event ID and strike of two nodal planes are marked. (d-e) Geometrical comparison between seismically delineated faults and focal mechanisms. Linear structures (F1–F6, dashed line) fitted by earthquake subgroups, with strike angle θ marked. The projection distance for F1–F5 is within 0.2 km and for F6 is 0.5 km, respectively. Events used for fitting individual faults are colored differently. Focal mechanisms of M_L3+ events are plotted. The orientation of S_{Hmax} (N38°E) predicted from borehole breakouts is marked (Shen et al., 2019a).

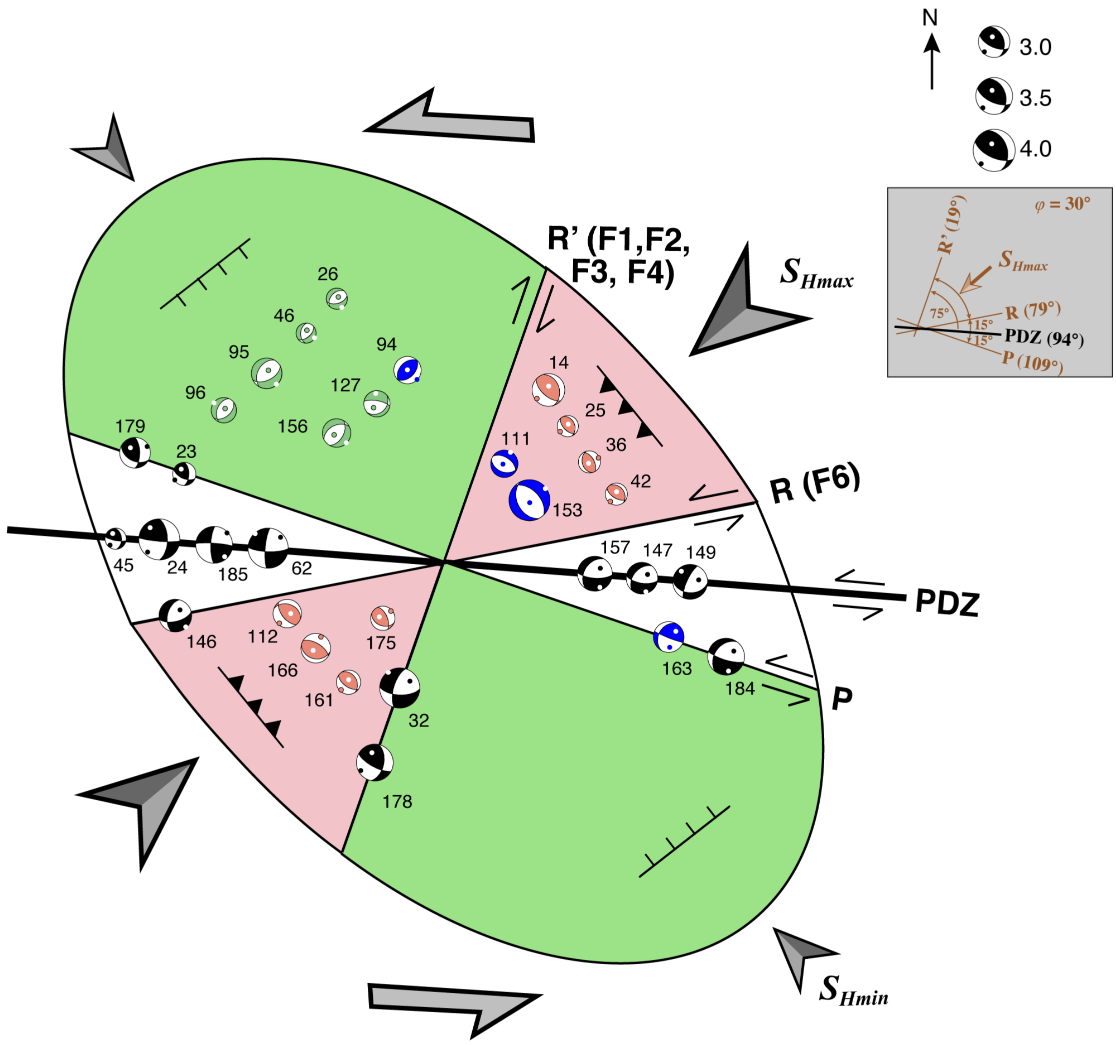

Figure 4. Fitted model of RSS with nodal planes of strike-slip focal mechanisms. The beach balls are listed according to the stress regime or the geometry of nodal planes. The color of beach balls is consistent with Fig. 3. Pink/Green areas: compression/tension zone. The orientation of structures is indicated on the top right panel.

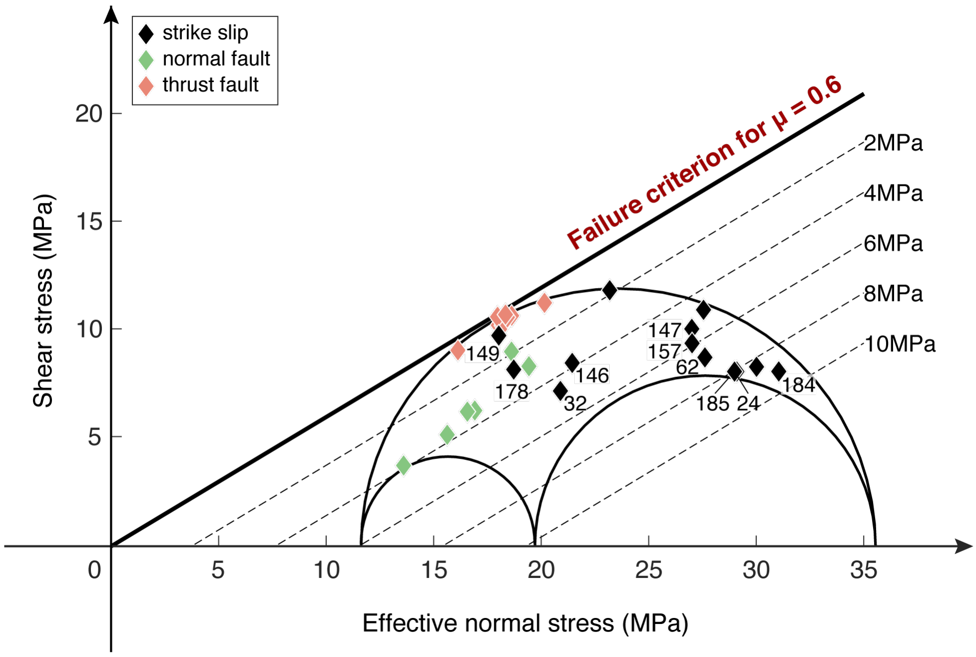

Figure 5. Mohr-Coulomb failure stress analysis. Mohr circle: stress conditions in the study area. Black diamonds mark stress state of strike slip events, assuming ruptured along the preferred nodal plane indicated in Fig. 4. Event ID of M_L3+ events are marked. Green and pink diamonds mark stress state of normal and thrust fault events, respectively, assuming the nodal plane closer to failure as the fault plane. Dashed lines are reference lines of ΔCFS required towards failure.

Table 1. Evaluation of E–W striking and N–S striking RSS models. Check marks: the model has a better performance/consistency and is preferred. Question marks: the model is not preferred but still acceptable. Cross mark: the model does not fit well. Specific information is detailed in the context. BH: borehole.

Factors	**RSS models**	
	E–W striking	N–S striking
Fitting performance (RMS)	✓	?
Reactivation of RSS sub-structures	✓	?
Consistency with epicentral delineated faults	✓	×
Consistency with S_{Hmax} from BH measurements	?	✓
Required stress perturbations (ΔCFS)	?	✓
High-resolution structures in the WCSB	✓	✓